Journal of Computational Physics **167,** 177–195 (2001)
doi:10.1006/jcph.2000.6666, available online at http://www.idealibrary.com on IDEAL®

Two-Dimensional Riemann Solver for Euler Equations of Gas Dynamics

M. Brio,* A. R. Zakharian,† and G. M. Webb‡

*Department of Mathematics, †ACMS, Department of Mathematics, University of Arizona, and ‡Lunar and Planetary Laboratory, University of Arizona, Tucson, Arizona 85721
E-mail: brio@math.arizona.edu, armis@acms.arizona.edu, cosray@lpl.arizona.edu

Received June 15, 1999; revised February 22, 2000

We construct a Riemann solver based on two-dimensional linear wave contributions to the numerical flux that generalizes the one-dimensional method due to Roe (1981, *J. Comput. Phys.* **43**, 157). The solver is based on a multistate Riemann problem and is suitable for arbitrary triangular grids or any other finite volume tessellations of the plane. We present numerical examples illustrating the performance of the method using both first- and second-order-accurate numerical solutions. The numerical flux contributions are due to one-dimensional waves and multidimensional waves originating from the corners of the computational cell. Under appropriate CFL restrictions, the contributions of one-dimensional waves dominate the flux, which explains good performance of dimensionally split solvers in practice. The multidimensional flux corrections increase the accuracy and stability, allowing a larger time step. The improvements are more pronounced on a coarse mesh and for large CFL numbers. For the second-order method, the improvements can be comparable to the improvements resulting from a less diffusive limiter.

Key Words: Godunov-type schemes; conservation laws; two-dimensional Riemann problem.

1. INTRODUCTION

In the past decade there have been numerous investigations of the use of linear solvers to account for the multidimensional nature of hyperbolic problems. The main advantages of such methods are an improved stability, resolution properties, and preservation of the directionally unsplit nature of the schemes [4, 11]. In particular, the adaptations of one-dimensional solvers in preferred directions were studied in [5, 12, 16–18]. The use of Lax–Wendroff type construction to include the cross derivative terms, which are in turn discretized by using a one-dimensional solver, was done by LeVeque [11]. Collela [4] used the corner transport upwinding method based on the predictor–corrector time integration in

0021-9991/01 $35.00

which predictor and corrector steps use different coordinate directions. Theoretical studies of two-dimensional Riemann problems for both scalar equations and Euler's equations were carried out in [3, 13, 20]. Genuine two-dimensional solvers were considered in [1] using the self-similar form of Euler's equations, leading to a mixed hyperbolic–elliptic problem. In [8] the formulas were derived for the linear 2-D Riemann problem for a subsonic case of gas dynamics and rectangular initial conditions. The Method of Transport that does not use a Riemann problem was introduced in [6, 7]. It relies on the assumption that flux contributions of separate waves can be decoupled and uses multidimensional waves transported from infinitely many propagation directions.

Our motivation to use a multistate Riemann problem came from previous studies of the weak shock reflection problem, a problem that may be interpreted as a multistate Riemann problem [2, 10].

In this paper, we construct a Riemann solver based on two-dimensional linear wave contributions to the numerical flux. The resulting numerical flux can be viewed as a one-dimensional flux normal to the cell boundaries plus the correction terms resulting from the waves emanating from the corners, which are computed using a multistate linear Riemann solver. The formulas generalize results obtained in [8] for arbitrary angles and for all the waves.

For small CFL numbers the contributions of one-dimensional waves dominate the flux, which explains a good performance of direction-split solvers in practice. The multidimensional flux corrections increase the stability, allowing large time steps and accuracy, although the improvements are often marginal. The overall efficiency may increase or decrease depending on the problem, on grids, and on the choice of the multidimensional method.

In the following section, the finite volume formulation on a hexagonal and rectangular grid is discussed. A detailed construction of the two-dimensional linear Riemann solver is described for the Euler equations of gas dynamics in Section 3. Numerical examples illustrating the performance of the method, including a second-order-accurate version on regular rectangular as well as hexagonal Delaunay–Voronoi dual meshes, are presented in Section 4.

In the Appendix we derive the analytical solution to a multistate linear Riemann problem for the Euler equations of gas dynamics.

2. THE FINITE VOLUME FLUX COMPUTATION

In this section we describe the use of the linear multistate Riemann solver in the simple case involving three-state initial data in a cell-centered finite volume method on a hexagonal grid. An example of such a grid, a regular Delaunay–Voronoi dual mesh, is shown in Fig. 1. Consider an integral form of a system of hyperbolic conservation laws

$$\frac{d}{dt}\int_A u\,dS + \int_\Gamma \mathbf{f}\cdot\mathbf{n}\,dl = 0, \tag{1}$$

where u is one of the conserved variables, A and Γ represent the volume and the boundary of the control region, and $\mathbf{n}$ is the outward normal to the cell. Integrating in time and over the computational cell, shown in Fig. 1, gives the finite volume approximation,

$$u_{ij}^{n+1} = u_{ij}^{n} - \frac{1}{A}\sum_k \int_0^{\Delta t} dt \int_{\Gamma_k} \mathbf{f}\cdot\mathbf{n}\,dl, \tag{2}$$

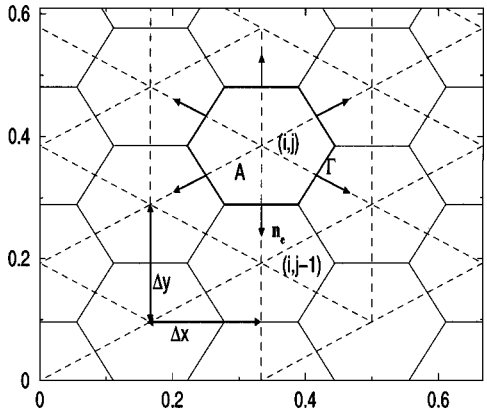

FIG. 1. Control volume of a dual Delaunay–Voronoi hexagonal mesh.

where u_{ij}^n represents the cell average at time t_n and Γ_k is the length of the edge of the computational cell. The cell averages are assumed to be given, while the fluxes are approximated using the values on the edge computed as solutions to the 3- and 2-state linear Riemann problems.

The initial data needed to determine the values of the flux density $\mathbf{f}$ along one of the edges consist of four states, as shown in Fig. 2.

The circles in this figure represent positions of the sonic wave fronts based on the average sound speed of the three surrounding states. The centers of the sonic circles are shifted by the position vector $-\bar{\mathbf{u}}\Delta t$ to account for the advection with average velocity $\bar{\mathbf{u}}$. Thus, the numerical flux across the sections of the edge, denoted by e_1, e_3, results from multidimensional waves originating from the corners of the computational cell. These fluxes are approximated using solutions to the 3-state linear Riemann problems described in the Appendix. For example, in Fig. 2, the flux across the section e_1 is computed as $\mathbf{f}(\mathbf{u}^*(x, y, t))$, where $\mathbf{u}^*(x, y, t)$ is the solution of the 3-state Riemann problem with the initial data from the cells O_1, O_2, and O_3. The flux across the section e_2 is determined only by the states O_2 and O_3 and can be computed using a 1-D Riemann solver. The resulting numerical flux

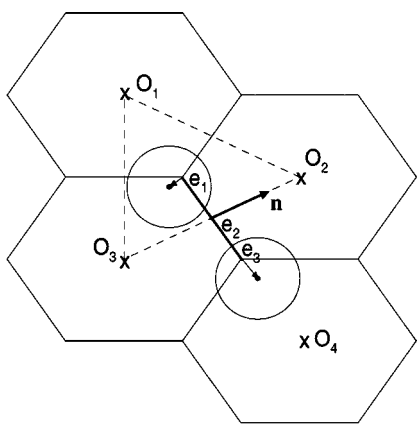

FIG. 2. Flux computation using three-state Riemann problems.

can be viewed as a one-dimensional flux across the cell boundaries plus the corrections resulting from the waves emanating from the corners.

The linear system that is solved in the linearization cell, shown in Fig. 2 in dashed lines, is of the form

$$U_t + \bar{A}U_x + \bar{B}U_y = 0, \tag{3}$$

where U is the perturbed state vector and the matrices $\bar{A}$ and $\bar{B}$ are the Jacobian matrices of the physical fluxes. They are evaluated at an intermediate state $\bar{U}$. This state $\bar{U}$ is a convex combination of the surrounding states shown in Fig. 2,

$$\bar{U} = \omega_1 U_1 + \omega_2 U_2 + \omega_3 U_3, \tag{4}$$

with $0 \le \omega_i \le 1$, $i = 1, 2, 3$, and $\omega_1 + \omega_2 + \omega_3 = 1$. In the numerical experiments presented in Section 4 we used uniform weighting. The Roe-type weights [9] did not produce any difference in our examples. To integrate the flux density function in each section, we have found the midpoint quadrature rule to be adequate in practice.

The procedure for the flux computation based on piecewise constant initial data, results in the scheme that is only first-order accurate in space. To extend the scheme to second order, we employ a MUSCL-type [19] approach, in particular the variant of the two-dimensional van Leer–Hancock scheme as described in [9]. First, the gradients in each computational cell are estimated and the values of the primitive variables, density, velocity, and pressure (denoted by w) are reconstructed as, e.g.,

$$w(x, y) = w(x_c, y_c) + \phi \nabla w \, \mathbf{dr}, \tag{5}$$

at cell boundaries, where $\mathbf{dr}$ is the distance from the cell center to the point on the edge, and ϕ is a limiter described below. Then the gradients $\nabla w = (\nabla w_x, \nabla w_y)$ in each cell are predicted using the discretization of the Green's formula

$$\nabla w \cong \frac{1}{A} \int_A \mathbf{n} \nabla w \, dS = \frac{1}{A} \int_\Gamma \mathbf{n} w \, dl \cong \frac{1}{A} \sum_{e \subset \Gamma} |e| w_e \mathbf{n}_e, \tag{6}$$

where summation is over a cell boundary, $|e|$ is the edge length, and the values w_e on the edge are averages of the neighboring cells as illustrated in Fig. 1,

$$w_e = \frac{w_{i,j} + w_{i,j-1}}{2}. \tag{7}$$

Alternatively, the gradient can be computed using the path of integration going through the surrounding cell centers. Both approaches are centered with respect to the cell center and result in second-order-accurate approximation of the gradient [9]. We used the latter approach in the numerical examples in Section 4. To avoid developing oscillations in the solution, the gradients are multiplied by the limiter. Here we use a minmod-type limiter as defined in [14]:

$$\phi = \min \begin{cases} 1 \\ \min_k \left(\frac{|w_k - \max_{path}(w_k)|}{|w_k - \max_{cell}(w_k)|} \right) \\ \min_k \left(\frac{|w_k - \min_{path}(w_k)|}{|w_k - \min_{cell}(w_k)|} \right). \end{cases}$$

Here index k runs over the components of the primitive variable state vector, so there is one limiter for all variables. The minimum and maximum over the path are found by examining the values on the edge used in the gradient evaluation sum in (6); the maximum and minimum over the cell are found by comparing values at the cell corners that are approximated using linear interpolation (5) without the limiter, $\phi = 1$. For the configuration shown in Fig. 2 predicted values are calculated at the cell face center for the 1-D Riemann problem, and at the cell corners for 3-state 2-D Riemann problems. For the second-order-accurate time integration, the solution is first updated to time $t + \frac{\Delta t}{2}$ using the first-order scheme

$$u_{ij}^{n+1/2} = u_{ij}^{n} - \frac{\Delta t}{2A} \sum_{k} \Gamma_k \Phi_k^n, \tag{8}$$

where Φ_k denotes approximation to the flux through the kth edge. Then these values are used in the prediction and limitation procedure described above. The final solution is obtained using fluxes computed from the Riemann problems based on these predicted values,

$$u_{ij}^{n+1} = u_{ij}^{n} - \frac{\Delta t}{A} \sum_{k} \Gamma_k \Phi_k^{n+1/2}. \tag{9}$$

3. THE MULTISTATE LINEAR RIEMANN SOLVER

Consider two-dimensional Euler equations linearized with respect to a constant background state, $\bar{U} = (\bar{\rho}, \bar{\mathbf{u}}, \bar{p})$, where the corresponding variables denote density, velocity $\bar{\mathbf{u}} = (\bar{u}, \bar{v})$, and pressure of the gas in a moving frame $x' = x - \bar{u}t$, $y' = y - \bar{v}t$.

The linearized Euler equations can be written in the moving frame as (dropping the primes)

$$\begin{aligned} \rho_t + \bar{\rho} \nabla \cdot \mathbf{u} &= 0, \\ \mathbf{u}_t + \nabla p / \bar{\rho} &= 0, \\ p_t + \bar{\rho} \bar{c}_s^2 \nabla \cdot \mathbf{u} &= 0, \end{aligned} \tag{10}$$

where $\bar{c}_s$ denotes the background sound speed.

The multistate piecewise constant initial data can be written as a superposition of data concentrated in a single wedge of arbitrary angle. Therefore it is sufficient to work out the formulas for one of the wedges shown in Fig. 2.

The solution can be thought of, in Fourier space, in terms of the eigenvalues and the eigenvectors of the matrix $ik_1\bar{A} + ik_2\bar{B}$, for Eq. (3), with k_1 and k_2 being the dual Fourier variables of x and y; or it can be thought of directly in physical space using well-known solution to the two-dimensional wave equation. Here we describe the latter approach.

Eliminating the velocity from the last two equations of the system (10) shows that the pressure satisfies the wave equation

$$\begin{aligned} p_{tt} - \bar{c}_s^2 \Delta p &= 0, \\ p(x, y, 0) &= p_0(x, y), \\ p_t(x, y, 0) &= -\bar{\rho} \bar{c}_s^2 \nabla \cdot \mathbf{u}(x, y, 0). \end{aligned}$$

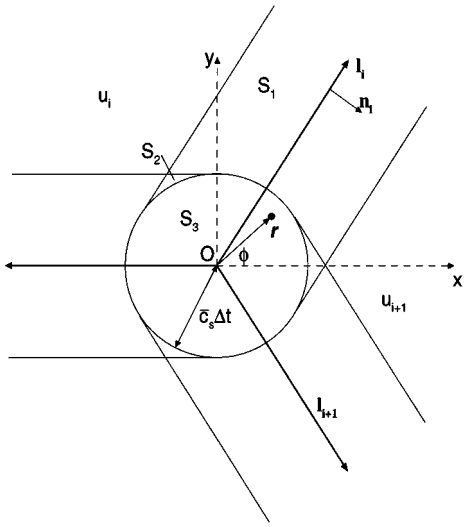

FIG. 3. Structure of a linear three-state 2-D Riemann problem.

The solution is given as a convolution in space of the initial data with the two-dimensional free space Green's function for the wave equation

$$p(x,y,t) = \frac{1}{2\pi\bar{c}_s}\frac{\partial}{\partial t}\int_\xi\int_\eta \frac{p_0(\xi,\eta)\,d\xi\,d\eta}{\sqrt{\bar{c}_s^2t^2-(x-\xi)^2-(y-\eta)^2}} - \frac{\rho\bar{c}_s}{2\pi}\int_\xi\int_\eta \frac{\nabla\cdot\mathbf{u}_0\,d\xi\,d\eta}{\sqrt{\bar{c}_s^2t^2-(x-\xi)^2-(y-\eta)^2}}, \tag{11}$$

where integration is over the area $(x-\xi)^2-(y-\eta)^2 \le \bar{c}_s^2t^2$.

The first integral in Eq. (11) gives an expression for the perturbation resulting from the initial piecewise constant pressure distribution. It is evaluated explicitly in the Appendix. The resulting expression depends on the number of crossings of the sonic circle, centered at the point of evaluation (x, y), with the discontinuity lines in the initial data as shown in Fig. 3. The second integral gives an expression for the pressure perturbation resulting from initial divergence of the piecewise constant velocity field. Note that the divergence at the origin, point O in Fig. 3, is zero since the velocity jumps stay finite across the discontinuity lines, while the surrounding area shrinks to zero.

Once the pressure is determined, the density can be computed noting that the first and the last equations of the system (10) imply

$$\rho(x,y,t) = \rho_0 + (p(x,y,t)-p_0)/\bar{c}_s^2. \tag{12}$$

The first term represents the advection of the initial density resulting from the entropy wave, while the second term is due to the acoustic waves.

Finally, the velocity can be computed by taking the gradient of the pressure followed by the integration in time,

$$\mathbf{u}(x,y,t) = \mathbf{u}(x,y,0) - \frac{1}{\bar{\rho}}\int_0^t \nabla p\,dt. \tag{13}$$

This equation accounts for both vorticity and acoustic mode contributions to u. To get back to the original frame of reference, x and y in the above formulas need to be replaced by $x - \bar{u}t$ and $y - \bar{v}t$, respectively.

4. NUMERICAL EXAMPLES

In this section, through numerical experiments, we illustrate the performance of the proposed method and compare it with other schemes. The experiments were done on regular rectangular and hexagonal grids. The flux integrals in (2) were approximated using the midpoint rule that requires single evaluation of the integrand. A constant ratio of specific heats, $\gamma = 1.4$, is used in all examples.

The first example is a two-dimensional Riemann problem with initial data consisting of two weak shocks and two slip lines,

$$\begin{array}{llll} \rho = 0.5313, & p = 0.4, & u = 0.0, & v = 0.0 \quad \text{if } x > 0, y > 0 \\ \rho = 1.0, & p = 1.0, & u = 0.0, & v = 0.7276 \quad \text{if } x > 0, y < 0 \\ \rho = 1.0, & p = 1.0, & u = 0.7276, & v = 0.0 \quad \text{if } x < 0, y > 0 \\ \rho = 0.8, & p = 1.0, & u = 0.0, & v = 0.0 \quad \text{if } x < 0, y < 0. \end{array}$$

At a later time, the solution was obtained using a second-order Roe-type method, with dimensional Strang splitting and superbee limiter on a 400×400 grid. It contains a Mach

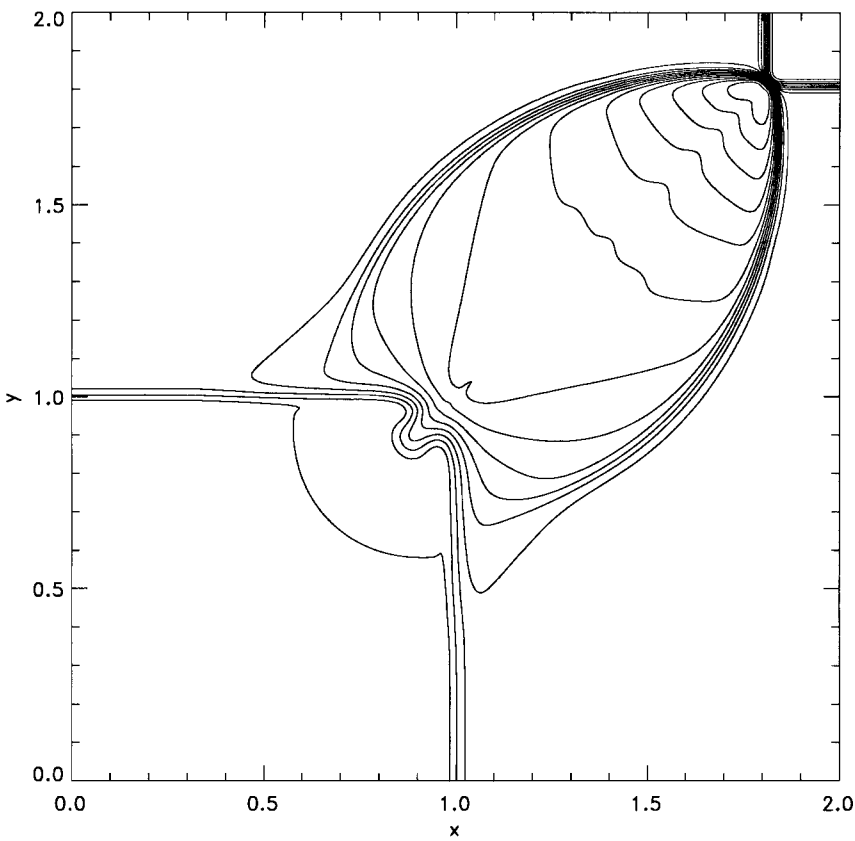

FIG. 4. Density, 400×400 hexagonal grid, CFL $= 0.5$, 1-D solver, $t = 0.52$.

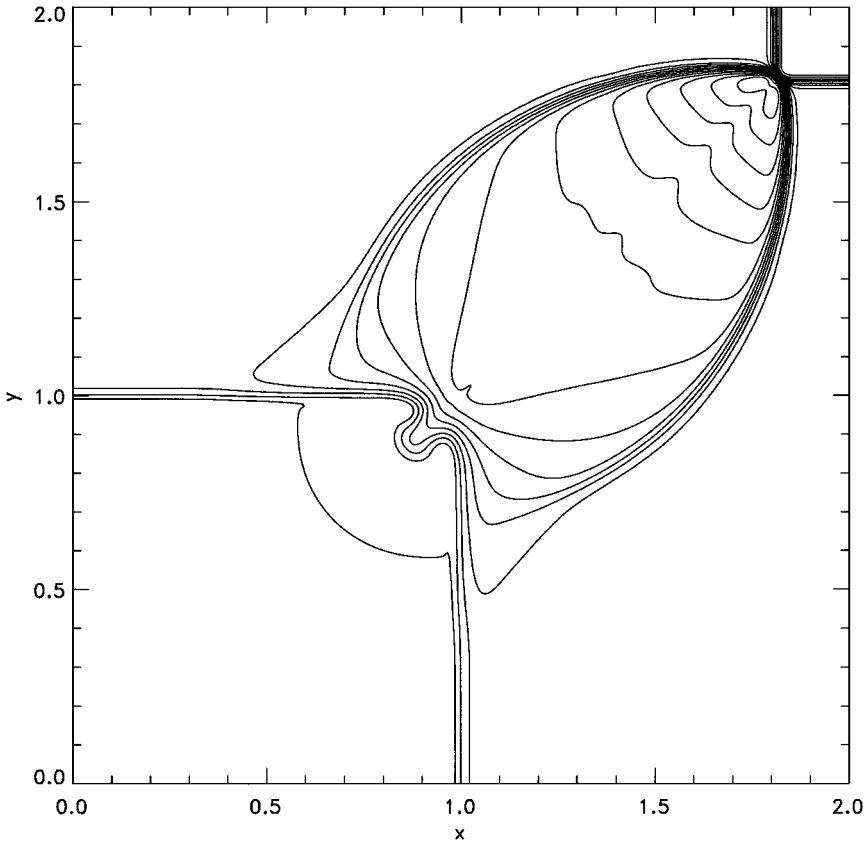

FIG. 5. Density, 400×400 hexagonal grid, CFL $= 0.5$, 2-D wave solver, $t = 0.52$.

reflection shown in Fig. 9. This case was analyzed in [6], where it was demonstrated that the van Leer flux vector splitting method may produce a curved shock connected with two other shocks, resembling regular shock reflection, while the multidimensional solver proposed in [6] is able to resolve the solution as a Mach reflection using the same number of grid points.

Similarly, we have observed a difference when using solver based on one-dimensional Riemann problems (2-state solver) computed in the directions normal to the cell edges and the solver based on the multistate Riemann problem. Figures 4 and 5 show the first-order solutions at time $t = 0.52$ obtained using each method with CFL $= 0.5$, where

$$CFL = \max[\max(|u| + c)\Delta t/\Delta x, \max(|v| + c)\Delta t/\Delta y]. \tag{14}$$

Computations in this case were done on a 400×400 equilateral hexagonal mesh, giving approximately the same Δx as on the rectangular grid of size 400×400 on the domain of size $[0, 2] \times [0, 2]$. Note that for such a hexagonal mesh $\Delta y = 2\Delta x/\sqrt{3}$. In the solution shown in Fig. 5, the region along the $x = y$ line is better resolved and is closer to the solution obtained using a second-order-accurate scheme. The same result, an improved resolution, is apparent when the first-order scheme on a rectangular grid of size 400×400 is used, as shown in Figs. 6 and 7. In this case the difference is more pronounced. This can be attributed to larger corrections because of a 4-state Riemann problem used at the cell corners on the rectangular grid as opposed to the 3-state configuration of the hexagonal case.

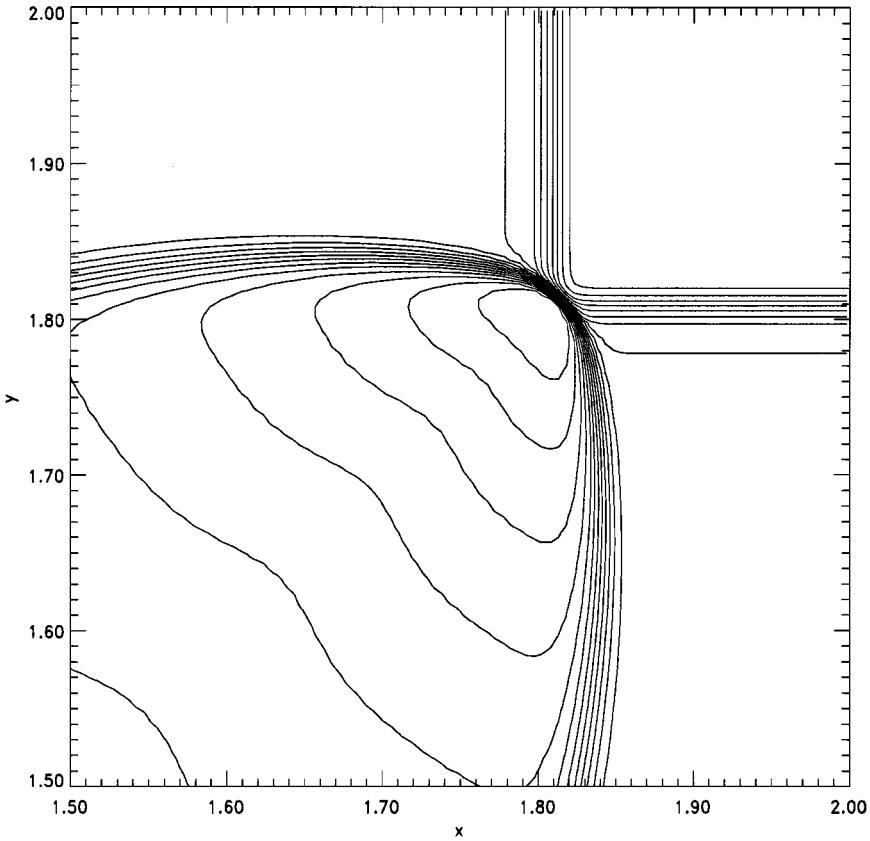

FIG. 6. Density, rectangular grid, CFL = 0.6, 1-D solver, $t = 0.52$, enlarged.

The difference between the two becomes more visible with increasing CFL numbers. The 2-state solver is stable up to CFL = 0.6, while the multistate solver can be run with CFL up to 1.0. Figure 8 shows the solution obtained using multistate solver with CFL = 1.0, and Fig. 9 is the solution obtained with the second-order method described above.

The second example is a radially symmetric Riemann problem in the form of a dense, high-pressure circle of gas with zero initial velocity,

$$\begin{aligned} \rho &= 2, \quad p = 15 \quad \text{if } r \le 0.13 \\ \rho &= 1, \quad p = 1 \quad \text{otherwise.} \end{aligned}$$

We have used a second-order scheme with the minmod-type limiter as outlined in Section 2. Figure 10 shows contour plots of the density at $t = 0.13$ computed using a 2-state linear solver on an 80×80 rectangular grid. The Courant number in this example is 0.7, which is the maximum for the 2-state solver. Figure 11 shows the solution to the same problem computed using multistate solver with CFL = 0.7 (maximum CFL in this case is 1.0). Figure 12 shows 1-D cuts along the $y = 0.5$ and $x = y$ lines compared with the highly resolved solution. It shows that the solution is more isotropic, and the radius of curvature of the shock at angles not aligned with grid lines is more uniform.

The next example is a two-dimensional Riemann problem that produces double Mach reflection and a shock propagating at the angle to the grid lines. Initial data in the four

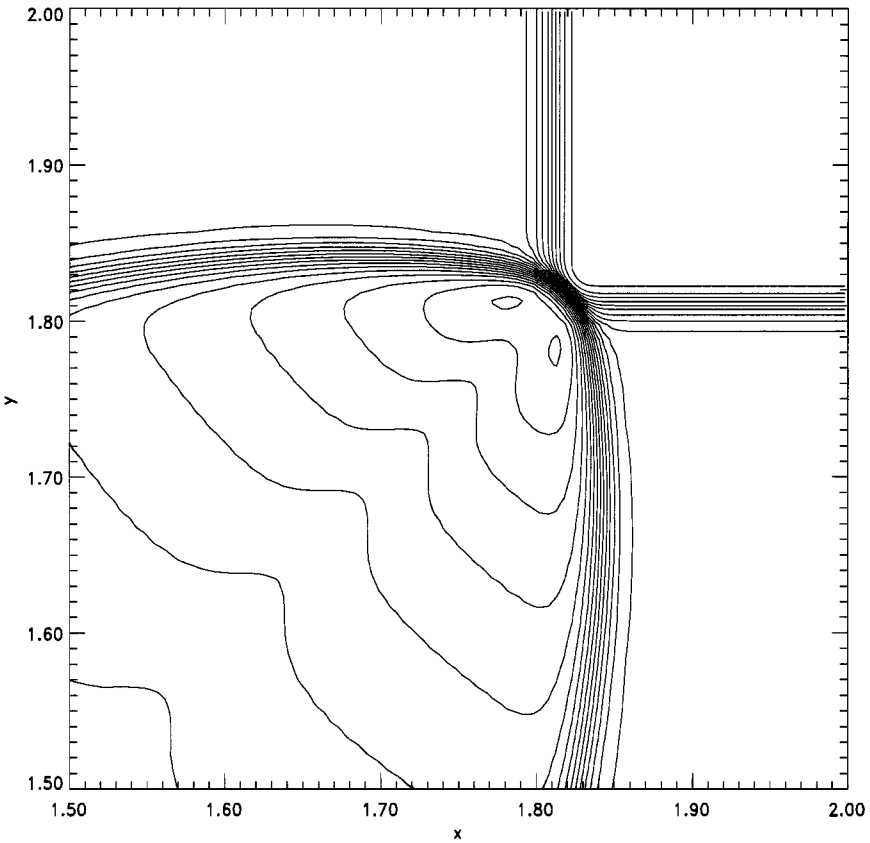

FIG. 7. Density, rectangular grid, CFL = 0.6, 2-D wave solver, $t = 0.52$, enlarged.

quadrants are given by, e.g., [11],

$$\begin{aligned}
&\rho = 1.5, \quad p = 1.5, \quad u = 0.0, \quad v = 0.0 \quad \text{if } x > 0, y > 0\\
&\rho = 0.5323, \quad p = 0.3, \quad u = 0.0, \quad v = 1.206 \quad \text{if } x > 0, y < 0\\
&\rho = 0.5323, \quad p = 0.3, \quad u = 1.206, \quad v = 0.0 \quad \text{if } x < 0, y > 0\\
&\rho = 0.1379, \quad p = 0.029, \quad u = 1.206, \quad v = 1.206 \quad \text{if } x < 0, y < 0.
\end{aligned}$$

Solutions for this case were computed on a 400×400 rectangular grid to time $t = 0.6$ using a second-order-accurate scheme and CFL $= 0.5$. Figures 13 and 14 demonstrate the difference in the resolution and position of the mushroom cap that forms due to the interaction of the dense stream and postshock flow behind the oblique shock. The solution obtained using the multistate solver is closer to the high-resolution solutions in [11] computed with the less diffusive monotonized central-difference and superbee limiters. Note that for the second-order scheme the change in the amount of the numerical diffusion due to different limiters may be comparable to the difference between the methods with and without 2-D wave corrections.

The multistate solver adds two additional flux calculations per cell edge. In addition, for second-order accuracy in time, the multistage integration was used. The number of expensive function evaluations used in the multistate solver varies depending on the problem. Overall efficiency (CPU time required to achieve the same quality of the solution) ranged

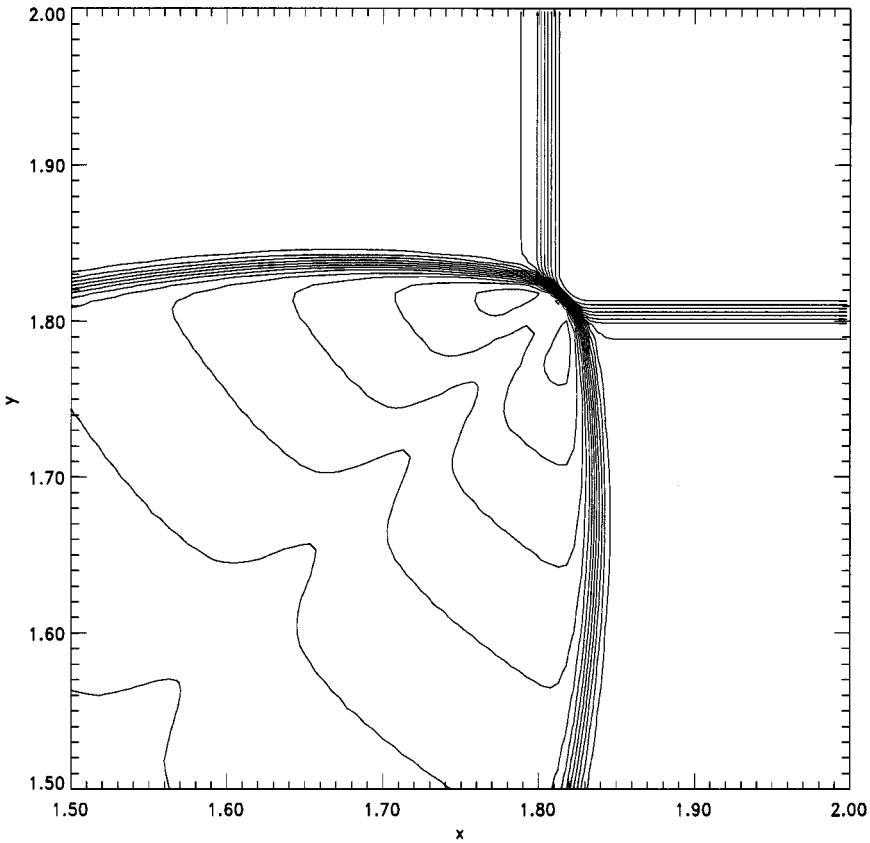

FIG. 8. Density, rectangular grid, CFL = 1.0, 1-D solver, $t = 0.52$, enlarged.

from 100% improvement in the first example to 50% decrease for the third example. In comparison, CLAWPACK is based on Lax–Wendroff-type time differencing with transverse wave propagation and requires three one-dimensional Riemann problems per interface, with only a single time update. It is also more cost efficient. Solvers that do not require solution of the Riemann problems, such as kinetic and flux-vector splitting schemes, are generally several times less expensive. In addition, for such solvers, increased cost of only 20% due to multidimensional corrections was reported by Fey [6].

5. CONCLUSIONS

In this paper we have obtained an exact solution of the multistate Riemann problem in two dimensions for the linearized Euler equations of gas dynamics and have utilized it in the construction of a numerical scheme. The numerical flux in our scheme generalizes the one-dimensional flux by introducing multidimensional wave contributions from the corners of the computational cell. These waves are computed using a multistate linearized Riemann problem and the formulas are suitable for finite volume applications on arbitrary grids.

The numerical experiments demonstrate that the additional information improves stability and reduces numerical diffusion of the scheme. The effect becomes more pronounced for large CFL numbers. The method also reduces anisotropy of the numerical diffusion and the grid alignment of the numerical solution.

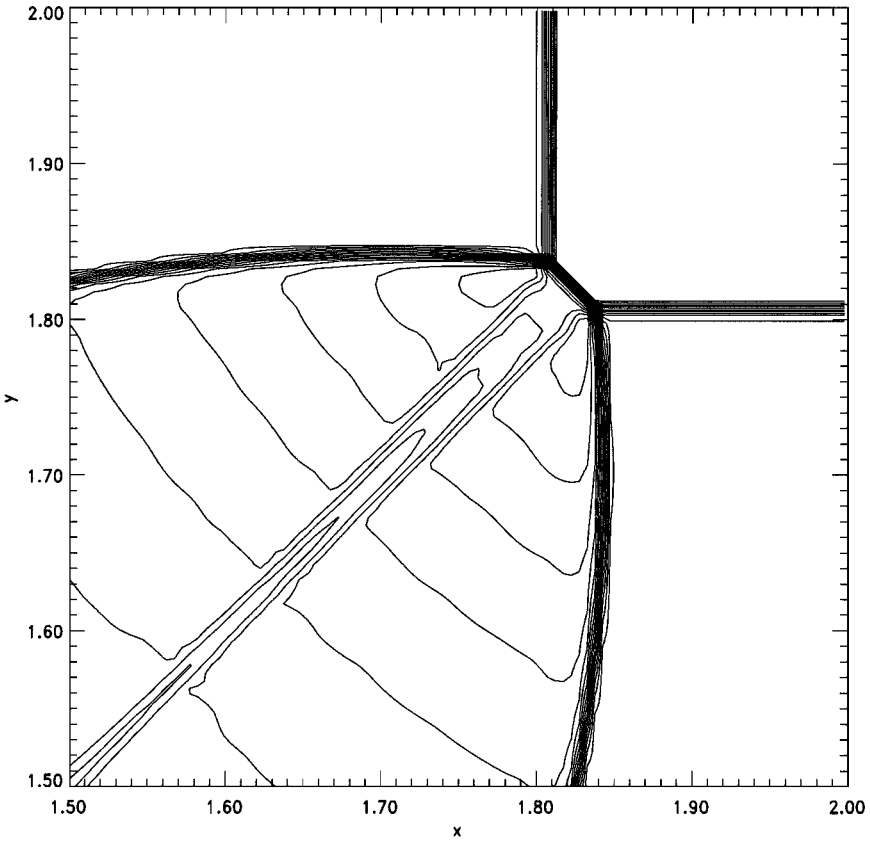

FIG. 9. Density, rectangular grid, second-order resolved solution, $t = 0.52$, enlarged.

APPENDIX

In this appendix we describe in more detail solution of a linear multistate Riemann problem. In particular we calculate the integrals in the expression (11) for the pressure, p. Since the problem is linear, the solution can be written as a superposition of the data concentrated in a single sector of arbitrary angle. Therefore it is sufficient to work out the formulas for one of the sectors.

First we note that for the region S_1, shown in Fig. 3, the initial value problem reduces to the one-dimensional wave equation for both pressure and velocity, and the solution can be written as

$$
\begin{aligned}
p(\mathbf{r}, t) &= p(\mathbf{r}, 0) + \frac{1}{2}[\mathrm{sign}[\sin(\phi - \phi_i)]\Delta p_i + \overline{\rho c_s}(\mathbf{n}_i \cdot \Delta \mathbf{u}_i)], \\
\mathbf{u}(\mathbf{r}, t) &= \mathbf{u}(\mathbf{r}, 0) + \frac{1}{2}\mathbf{n}_i \left[\frac{\Delta p_i}{\overline{\rho c_s}} + \mathrm{sign}[\sin(\phi - \phi_i)](\mathbf{n}_i \cdot \Delta \mathbf{u}_i) \right], \\
\rho(\mathbf{r}, t) &= \rho(\mathbf{r}, 0) + (p(\mathbf{r}, t) - p(\mathbf{r}, 0))/\overline{c_s^2},
\end{aligned}
\tag{1}
$$

where index i corresponds to the line of discontinuity $\mathbf{l}_i = (\cos(\phi_i), \sin(\phi_i))$ in the initial data, $\Delta p_i = p_{i+1} - p_i$, and $\Delta \mathbf{u}_i = \mathbf{u}_{i+1} - \mathbf{u}_i$. Position vector $\mathbf{r} = (x, y) = (r\cos(\phi), r\sin(\phi))$ refers to the origin at the point O, $\mathbf{n}_i = (-\sin(\phi_i), \cos(\phi_i))$ is the unit normal to

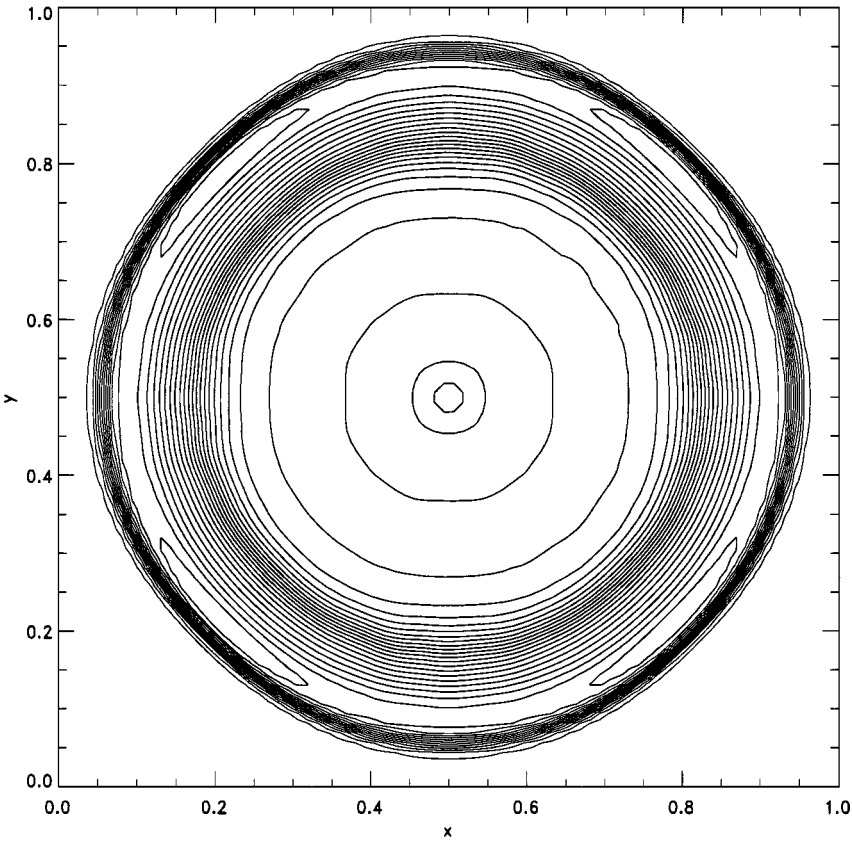

FIG. 10. Density plot for the radially symmetric Riemann problem, 80×80 rectangular grid, CFL $= 0.7$, 1-D solver, $t = 0.13$.

the line l_i. For region S_2 (see Fig. 3), the solution is a superposition of the corresponding one-dimensional waves.

For region S_3 the solution to the wave equation for pressure can be written as

$$p(x, y, t) = \frac{1}{2\pi \bar{c}_s} \frac{\partial}{\partial t} \int_\xi \int_\eta \frac{p_0(\xi, \eta)\, d\xi\, d\eta}{\sqrt{\bar{c}_s^2 t^2 - (x-\xi)^2 - (y-\eta)^2}} \tag{2}$$

$$- \frac{\rho \bar{c}_s}{2\pi} \int_\xi \int_\eta \frac{\nabla \cdot \mathbf{u}_0\, d\xi\, d\eta}{\sqrt{\bar{c}_s^2 t^2 - (x-\xi)^2 - (y-\eta)^2}}, \tag{3}$$

where integration is over the area $(x-\xi)^2 - (y-\eta)^2 \le \bar{c}_s^2 t^2$. Consider the first integral in the expression above, converted to polar coordinates,

$$\begin{aligned}
&\frac{1}{2\pi \bar{c}_s} \frac{\partial}{\partial t} \int_\xi \int_\eta \frac{p_0(\xi, \eta)}{\sqrt{\bar{c}_s^2 t^2 - (x-\xi)^2 - (y-\eta)^2}}\, d\xi\, d\eta \\
&\quad = p_0(x, y) + \frac{1}{2\pi \bar{c}_s} \frac{\partial}{\partial t} \int_\xi \int_\eta \frac{p_0(\xi, \eta) - p_0(x, y)}{\sqrt{\bar{c}_s^2 t^2 - (x-\xi)^2 - (y-\eta)^2}}\, d\xi\, d\eta \\
&\quad = p_0(x, y) + \frac{1}{2\pi \bar{c}_s} \frac{\partial}{\partial t} \int_0^{2\pi} \int_0^{r_+} \frac{\Delta p_0(\phi') r'}{\sqrt{-r'^2 + 2\cos(\phi' - \phi) r r' + \bar{c}_s^2 t^2 - r^2}}\, dr'\, d\phi',
\end{aligned}$$

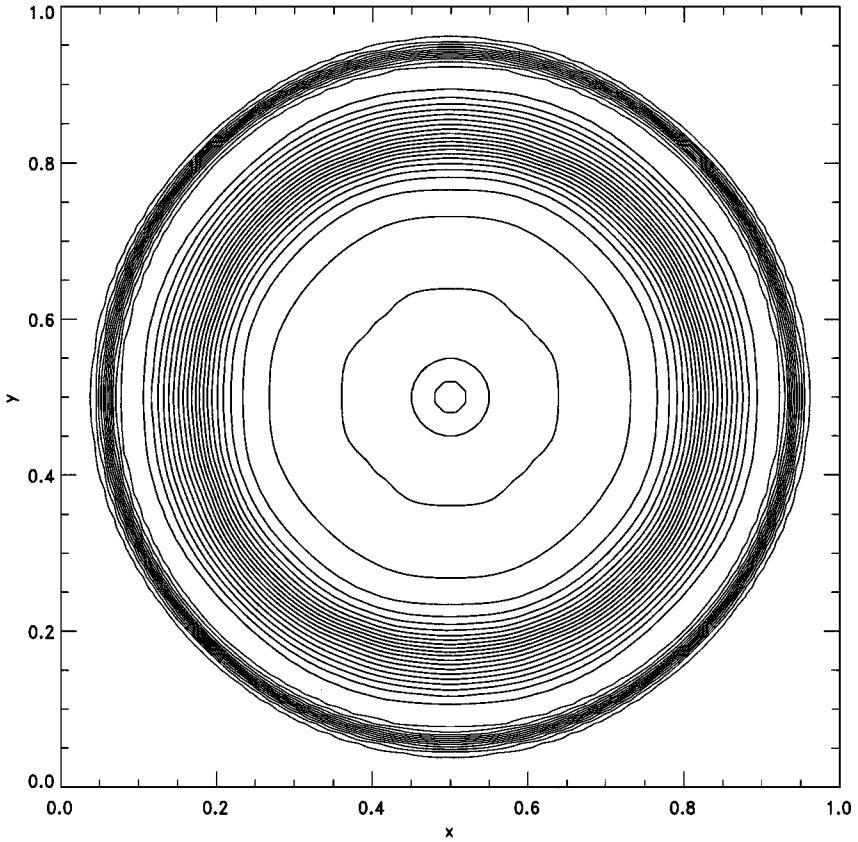

FIG. 11. Density plot for the radially symmetric Riemann problem, 80×80 rectangular grid, CFL $= 0.7$, 2-D wave solver, $t = 0.13$.

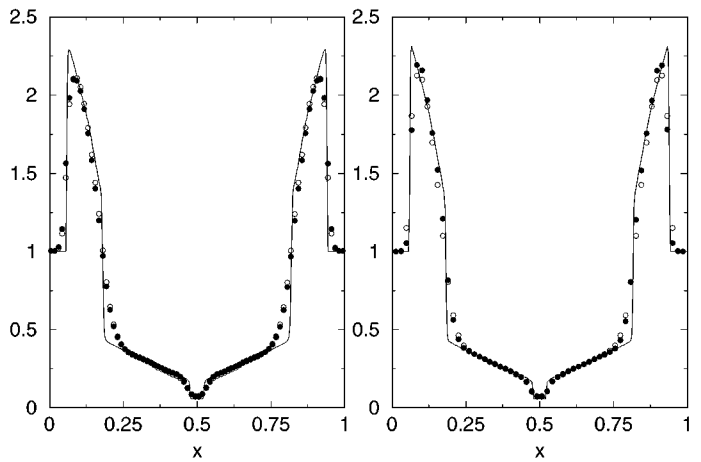

FIG. 12. Comparison of the resolved solution (solid lines), computed on a 400×400 grid with a second-order scheme and superbee limiter, and solutions obtained on an 80×80 grid using two-state (filled circles) and multistate (open circles) solvers. Left panel shows cuts along the $y = 0.5$ line; right panel shows cuts along the $x = y$ line.

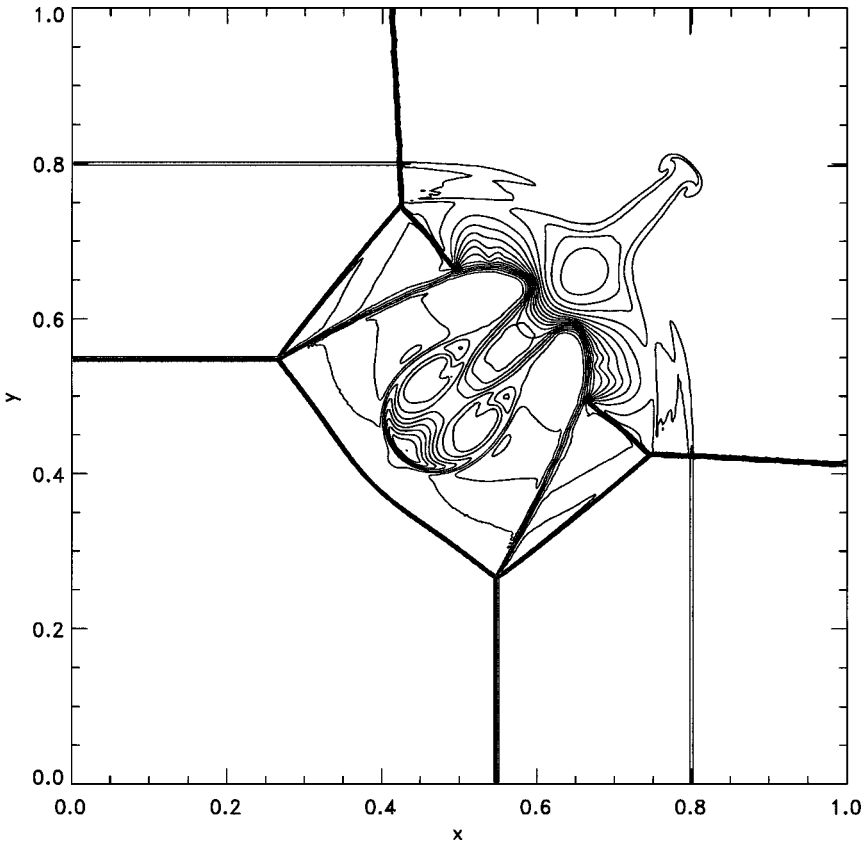

FIG. 13. Density, double Mach reflection problem, 400 × 400 rectangular grid, 1-D solver, $t = 0.6$.

where r_+ is the distance between the evaluation point (x, y) and the sonic wave front,

$$r_+ = r\cos(\phi' - \phi) + \sqrt{\bar{c}_s^2 t^2 - r^2 \sin^2(\phi - \phi')}.$$

Integration with respect to r' gives

$$\int_0^{r_+} \frac{r'}{\sqrt{-r'^2 + 2\cos(\phi' - \phi) r r' + \bar{c}_s^2 t^2 - r^2}}\, dr'$$
$$= \sqrt{\bar{c}_s^2 t^2 - r^2} + r\cos(\phi' - \phi)\left(\frac{\pi}{2} + \arctan\frac{r\cos(\phi' - \phi)}{\sqrt{\bar{c}_s^2 t^2 - r^2}}\right).$$

Dropping the term that is independent of the time and integrating with respect to ϕ' we get

$$\int_{\phi_i}^{\phi_{i+1}} \left(\sqrt{\bar{c}_s^2 t^2 - r^2} + (r\cos(\phi' - \phi))\arctan\frac{r\cos(\phi' - \phi)}{\sqrt{\bar{c}_s^2 t^2 - r^2}}\right) d\phi'$$
$$= r\sin(\phi - \phi')\arctan\frac{r\cos(\phi' - \phi)}{\sqrt{\bar{c}_s^2 t^2 - r^2}}\Bigg|_{\phi_i}^{\phi_{i+1}} + c_s t \arctan\left(\sqrt{1 - \frac{r^2}{\bar{c}_s^2 t^2}}\tan(\phi - \phi')\right)\Bigg|_{\phi_i}^{\phi_{i+1}}.$$

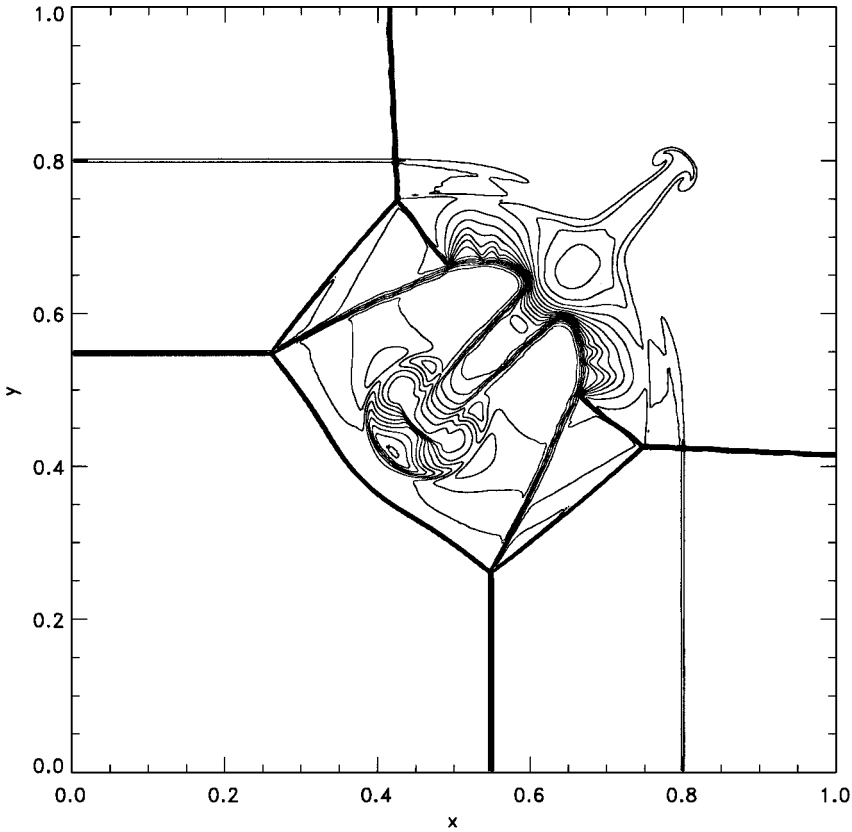

FIG. 14. Density, double Mach reflection problem, 400×400 rectangular grid, 2-D wave solver, $t = 0.6$.

The second term is discontinuous at $\phi - \phi' = \pm\frac{\pi}{2}$ and therefore if it is within the limits of integration, it will contribute $\frac{\pi}{2}$ to the definite integral. Thus, the interval of integration is split into regions where both the initial data and antiderivative are continuous. Finally, taking the time derivative and summing over all initial states the integral in Eq. (2) becomes

$$\frac{1}{2\pi}\sum_{i=1}^{m} \Delta p_i F_i,$$

where F_i is

$$F_i = \frac{\pi}{2}(1 + \text{sign}[\cos(\phi_i - \phi)])\text{sign}[\sin(\phi - \phi_i)] - \arctan\left(\sqrt{1 - \frac{r^2}{\bar{c_s}^2 t^2}}\tan(\phi - \phi_i)\right).$$

The integral (3) in the expression for the pressure is a line integral along each of $\mathbf{l}_i$ and can be computed as

$$\frac{\rho\bar{c_s}}{2\pi}\int_\xi\int_\eta \frac{\nabla\cdot\mathbf{u}_0\, d\xi\, d\eta}{\sqrt{\bar{c_s}^2 t^2 - (x-\xi)^2 - (y-\eta)^2}}$$
$$= \frac{\rho\bar{c_s}}{2\pi}(\mathbf{n}_i\cdot\Delta\mathbf{u}_i)\int_0^{r_+(\phi_i)} \frac{1}{\sqrt{-r'^2 + 2\cos(\phi_i - \phi)rr' + \bar{c_s}^2 t^2 - r^2}}\, dr'$$

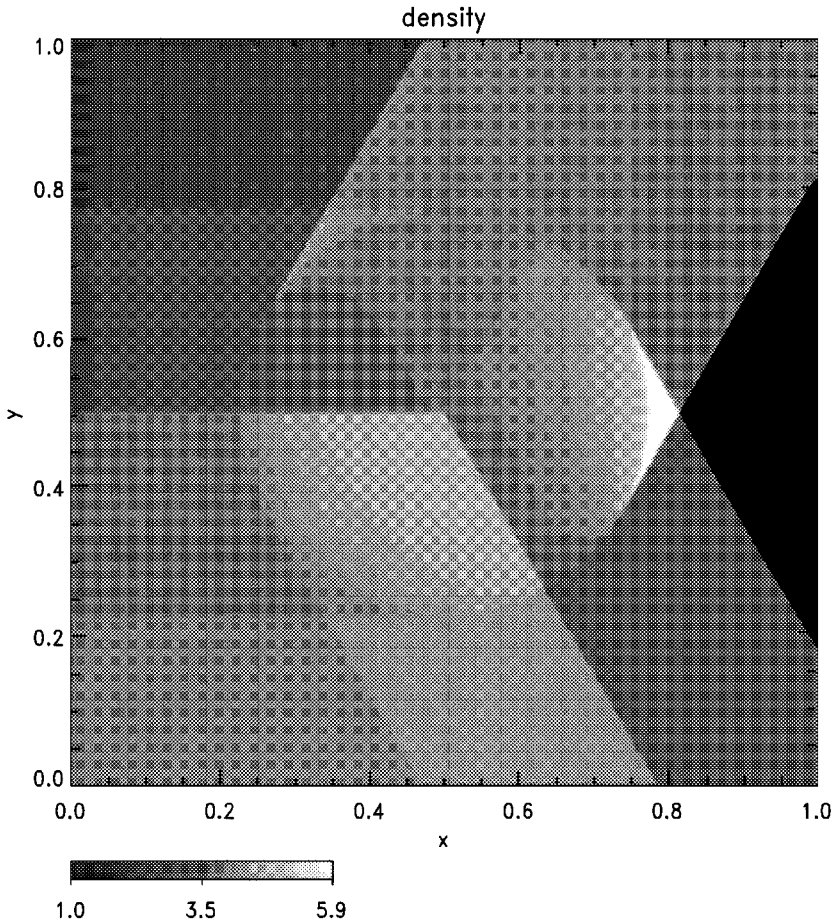

FIG. 15. Density, solution to the linear 2-D Riemann problem, $t = 0.15$.

$$= \frac{\rho\bar{c_s}}{2\pi}(\mathbf{n}_i \cdot \Delta\mathbf{u}_i)\left(\frac{\pi}{2} + \arctan\frac{r\cos(\phi_i - \phi)}{\sqrt{\bar{c_s}^2 t^2 - r^2}}\right)$$

$$= \frac{\rho\bar{c_s}}{2\pi}(\mathbf{n}_i \cdot \Delta\mathbf{u}_i)G_i,$$

where G_i is

$$G_i = \arctan\left(\frac{\mathbf{l}_i \cdot \mathbf{r}}{\sqrt{\bar{c_s}^2 t^2 - r^2}}\right) + \frac{\pi}{2}.$$

Combining formulas for (2) and (3) we obtain the pressure:

$$p(\mathbf{r}, t) = p(\mathbf{r}, 0) + \frac{1}{2\pi}\sum_{i=1}^{m}\Delta p_i F_i + \frac{\overline{\rho c_s}}{2\pi}\sum_{i=1}^{m}(\mathbf{n}_i \cdot \Delta\mathbf{u}_i)G_i.$$

To find velocity we take the gradient of the expression for p followed by integration in time. Applying this to the first integral (2) results in the expression (3), which was computed above, with $\nabla \cdot \mathbf{u}_0$ replaced by ∇p_0. That evaluates to the term proportional to $\Delta p_i G_i$.

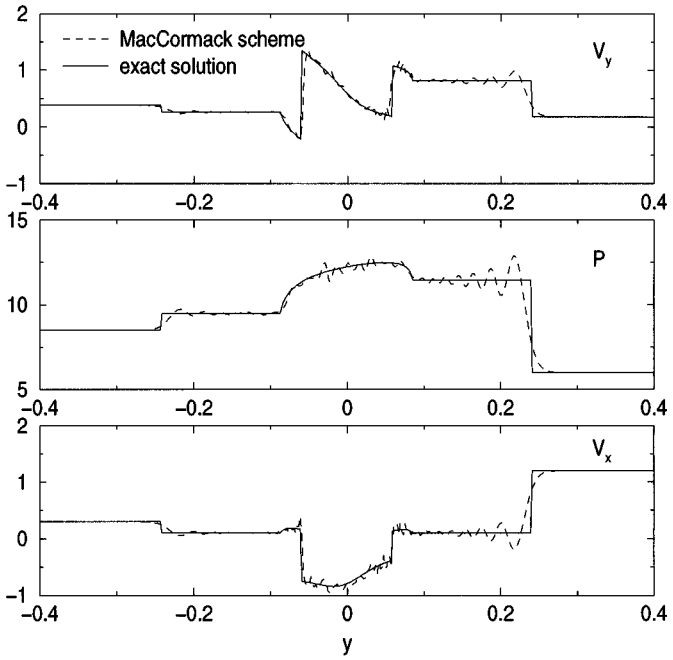

FIG. 16. Comparison of the exact and numerical solutions to the linear 2-D Riemann problem, $t = 0.05$.

Noting that the gradient and time integration of (3) can be carried out using an explicit formula for G_i, we obtain the expression

$$\mathbf{u}(\mathbf{r}, t) = \mathbf{u}(\mathbf{r}, 0) + \frac{1}{2\pi} \sum_{i=1}^{m} \begin{pmatrix} \mathbf{n}_i \cdot \mathbf{w}_i \\ \mathbf{l}_i \cdot \mathbf{w}_i \end{pmatrix},$$

where

$$\mathbf{w}_i = \begin{pmatrix} (\mathbf{n}_i \cdot \Delta\mathbf{u}_i) F_i + \frac{\Delta p_i}{\rho c_s} G_i \\ (\mathbf{n}_i \cdot \Delta\mathbf{u}_i) \log\left(\frac{r}{C_s t + \sqrt{C_s^2 t^2 - r^2}}\right) \end{pmatrix}.$$

The logarithmic term is due to the vorticity mode present in the initial data. Finally, the density can be determined as in (1).

The example in Fig. 15 shows the exact solution to the linear Riemann problem for density at $t = 0.15$, with the initial data consisting of three states,

$$\begin{aligned} &\rho = 2.0, \quad p = 6.0, \quad u = 1.2, \quad v = 0.18 \quad \text{if } y > 0 \text{ and } y > \sqrt{3}x \\ &\rho = 1.0, \quad p = 2.2, \quad u = -2.3, \quad v = 1.0 \quad \text{if } x > 0 \text{ and } |y| < \sqrt{3}x \\ &\rho = 4.0, \quad p = 8.5, \quad u = 0.3, \quad v = 0.38 \quad \text{if } y < 0 \text{ and } y < -\sqrt{3}x. \end{aligned}$$

Figure 16 is the exact solution of the pressure and velocity at $t = 0.05$ along the line $x = 0.03$ for the same problem together with the numerical solution obtained using MacCormack's scheme applied to the linearized Euler equations of gas dynamics.

ACKNOWLEDGMENT

The work of G.M.W. was supported in part by NASA Grant NAG5-5180.

REFERENCES

1. R. Abgrall, Approximation du problème de Riemann vraiment multidimensionnel des èquations d'Euler par une mèthode de type Roe, I: La linèarisation, *C.R. Acad. Sci. Ser. I* **319**, 499 (1994); 499–504; II: Solution du probleme de Riemann approchè, *C.R. Acad. Sci. Ser. I* **319**, 625.
2. M. Brio and J. K. Hunter, Mach reflection for the two-dimensional Burgers equation, *Physica D* **60**, 194 (1992).
3. T. Chang and L. Hsiao, *The Riemann Problem and Interaction of Waves in Gas Dynamics* (Wiley, New York, 1989).
4. P. Collela, Multidimensional upwind methods for hyperbolic conservation laws, *J. Comput. Phys.* **87**, 171 (1990).
5. S. F. Davis, A rotationally biased upwind difference schenme for Euler equations, *J. Comput. Phys.* **56**, 65 (1984).
6. M. Fey, Multidimensional upwinding. 1. The method of transport for solving the Euler equations, *J. Comput. Phys.* **143**, 159 (1998).
7. M. Fey, Multidimensional upwinding. 2. Decomposition of the Euler equations into advection equation, *J. Comput. Phys.* **143**, 181 (1998).
8. H. Gilquin, J. Laurens, and C. Rosier, Multi-dimensional Riemann problems for linear hyperbolic systems, *Notes Numer. Fluid Mech.* **43**, 284 (1993).
9. E. Godlewski and P.-A. Raviart, *Numerical Approximation of Hyperbolic Systems of Conservation Laws* (Springer-Verlag, New York, 1996).
10. S. Canic, B. L. Keyfitz, and D. H. Wagner, A bifurcation diagram for oblique shock interactions in the unsteady transonic small disturbance equation, in *Proceedings of the Fifth International Conference on Hyperbolic Problems: Theory, Numerics, Applications*, edited by J. Glimm *et al.* (World Scientific, Singapore, 1994).
11. R. J. LeVeque, Wave propagation algorithms for multidimensional hyperbolic systems, *J. Comput. Phys.* **131**, 327 (1997).
12. D. W. Levy, K. G. Powell, and B. van Leer, Use of rotated Riemann solver for two-dimensional Euler equations, *J. Comput. Phys.* **106**, 201 (1993).
13. W. B. Lindquist, The scalar Riemann problem in two spatial dimensions: piecewise smoothness of solutions and its breakdown, *SIAM J. Math. Anal.* **17**, 1178 (1986).
14. D. De Zeeuw and K. Powell, An adaptively refined cartesian mesh solver for the Euler equations, *J. Comput. Phys.* **104**, 56 (1993).
15. P. L. Roe, Approximate Riemann solvers, parameter vectors and difference schemes, *J. Comput. Phys.* **43**, 357 (1981).
16. P. L. Roe, Discrete models for the numerical analysis of time-dependent multidimensional gas dynamics, *J. Comput. Phys.* **63**, 458 (1986).
17. P. L. Roe, *Linear Advection Schemes on Triangular Meshes*, Tech. Rep. CoA, Rep. No. 8720 (Cranfield, 1987).
18. C. B. Rumsey, B. van Leer, and P. L. Roe, A multidimensional flux function with applications to the Euler and Navier–Stokes equations, *J. Comput. Phys.* **105**, 306 (1993).
19. B. van Leer, Towards the ultimate conservative difference scheme: V. A second order sequel to Godunov's method, *J. Comput. Phys.* **32**, 101 (1979).
20. D. H. Wagner, The Riemann problem in two space dimensions for a single conservation law, *SIAM J. Math. Anal.* **14**, 534 (1983).